

Tide-induced variability in beach surface moisture: Observations and modelling

Laura B. Brakenhoff,^{ID} Yvonne Smit,^{ID} Jasper J. A. Donker^{ID} and Gerben Ruessink*^{ID}

Department of Physical Geography, Faculty of Geosciences, Utrecht University, Utrecht, The Netherlands

Received 6 November 2017; Revised 11 July 2018; Accepted 16 August 2018

*Correspondence to: Gerben Ruessink, Department of Physical Geography, Faculty of Geosciences, Utrecht University, P.O. Box 80.115, 3508 TC Utrecht, The Netherlands. E-mail: B.G.Ruessink@uu.nl

This is an open access article under the terms of the Creative Commons Attribution License, which permits use, distribution and reproduction in any medium, provided the original work is properly cited.

ESPL

Earth Surface Processes and Landforms

ABSTRACT: The moisture content w_s of a beach surface strongly controls the availability of sand for aeolian transport. Our predictive capability of the spatiotemporal variability in w_s , which depends to a large extent on water table depth, is, however, limited. Here we show that water table fluctuations and surface moisture content observed during a 10-day period on a medium-grained (365 μm) planar (1:30) beach can be predicted well with the nonlinear Boussinesq equation extended to include run-up infiltration and a soil–water retention curve under the assumption of hydrostatic equilibrium. On the intertidal part of the beach the water table is observed and predicted to continuously fall from the moment the beach surface emerges from the falling tide to just before it is submerged by the incoming tide. We find that on the lower 30% of the intertidal beach the water table remains within 0.1–0.2 m from the surface and that the sand is always saturated ($w_s \approx 20\%$, by mass). Higher up on the intertidal beach, the surface can dry to about 5% when the water table has fallen to 0.4–0.5 m beneath the surface. Above the high-tide level the water table is always too deep (> 0.5 m) to affect surface moisture and, without precipitation, the sand is dry ($w_s < 5–8\%$). Because the water table depth on the emerged part of the intertidal beach increases with time irrespective of whether the (ocean) tide falls or rises, we find no need to include hysteresis (wetting and drying) effects in the surface-moisture modelling. Model simulations suggest that at the present planar beach only the part well above mean sea level can dry sufficiently ($w_s < 10\%$) for sand to become available for aeolian transport. ©2018 The Authors. Earth Surface Processes and Landforms published by John Wiley & Sons Ltd.

KEYWORDS: beach surface moisture; groundwater; sand engine; tidal variations

Introduction

Wind-blown sand transport from a beach constitutes the main sediment source into dunes, allowing them to grow and to recover after the erosive effects of marine processes during severe storm surges. Although a sufficiently strong wind is needed to initiate aeolian transport, model predictions of sand supply based on wind characteristics alone often grossly over-predict measured sand deposition in the dunes (e.g., Sarre, 1989; Davidson-Arnott and Law, 1996; Delgado-Fernandez, 2011; De Vries *et al.*, 2012; Keijsers *et al.*, 2014). Various beach surface properties have been proposed to limit sand supply. On nourished beaches coarse shell material often forms a lag deposit that prevents the underlying sand from becoming entrained (e.g., Van der Wal, 1998; De Vries *et al.*, 2014b), while on natural beaches surface moisture is commonly regarded as the main supply-limiting factor (e.g., Jackson and Nordstrom, 1997; Bauer and Davidson-Arnott, 2002; Wiggs *et al.*, 2004; Davidson Arnott *et al.*, 2008; Delgado-Fernandez, 2011; Poortinga *et al.*, 2015). Moisture raises the threshold velocity for the initiation of motion (e.g., Namikas and Sherman, 1995) and prohibits transport entirely when the moisture content at the bed surface exceeds about

10% by mass (e.g., Delgado-Fernandez, 2011). Also, moisture limits the pickup of sand grains into the saltation cascade once motion has started (Delgado-Fernandez, 2010). As a consequence, the aeolian transport rate at the beach–dune intersection is often substantially lower than estimated from transport equations that assume dry sand (Sherman *et al.*, 1998). While considerable progress has recently been made in measuring the temporal and spatial variability in surface moisture (e.g., Yang and Davidson-Arnott, 2005; Nield *et al.*, 2011; Smit *et al.*, 2018), practical models to predict this variability (e.g., Hoonhout and De Vries, 2016) are still in their infancy and must be improved and validated further as a precursor to quantitatively realistic aeolian sand-supply models.

Planar beaches can broadly be divided into three cross-shore moisture zones (Salvat, 1964; Pollock and Hummon, 1971; Yang and Davidson-Arnott, 2005; Bauer *et al.*, 2009; Namikas *et al.*, 2010; Schmutz, 2014). The surface moisture content w_s of the upper beach, above the high-tide level, is generally low ($w_s < 5\%$, by mass), with only small variations that are mostly ascribed to atmospheric processes such as evaporation (Namikas *et al.*, 2010; Schmutz, 2014). Further down, in the middle to upper intertidal zone, the beach moisture content is much more variable ($w_s \approx 5–25\%$),

from saturated immediately after the emersion of the beach surface during falling tide to nearly dry just before its submersion by the rising tide. Here, spatiotemporal moisture variations are often ascribed to variations in the depth h of the water table beneath the bed (e.g., Atherton *et al.*, 2001; Namikas *et al.*, 2010). Just above the low-tide level, where the groundwater table is shallowest ($h < 0.1 - 0.2$ m), the sand remains saturated. In this case, the capillary fringe above the water table intersects the surface (e.g., Namikas *et al.*, 2010; Schmutz and Namikas, 2013). On fine-11grained low-sloping beaches the water table can remain close to the surface for most of the tide and, accordingly, the persistently saturated part of the beach can extend well landward of the swash zone (Atherton *et al.*, 2001). Barred beaches exhibit the same overall increase in moisture content from the dry beach to the swash zone as on planar beaches but with superimposed topographic variability, with drier sand on the bars and wetter sand in the troughs (Oblinger and Anthony, 2008; Smit *et al.*, 2018). In this paper we focus on water table dynamics and associated surface moisture variability.

Beach water table fluctuations are driven primarily by tides and waves (set-up and run-up) (e.g., Pollock and Hummon, 1971; Lanyon *et al.*, 1982; Nielsen, 1990; Kang *et al.*, 1994; Baird *et al.*, 1998; Raubenheimer *et al.*, 1999; Horn, 2002; Huizer *et al.*, 2017), although rainfall can contribute too (Huisman *et al.*, 2011). Observations above the high-tide level, summarized in Lanyon *et al.* (1982) and Horn (2002), have shown that tide-induced water table fluctuations dampen in amplitude in the onshore direction, are markedly asymmetric in time (rapid rise and gentle fall) and have a mean that is well above the mean level of the ocean tide. This overheight fluctuates with the neap–spring tidal cycle (e.g., Raubenheimer *et al.*, 1999) and is enhanced by wave set-up and run-up (Turner *et al.*, 1997). Data from wells at seven cross-shore intertidal locations on a steep (1:10), coarse-sand (mean grain size $660 \mu\text{m}$) planar beach (Pollock and Hummon, 1971) show the water table to fall from emersion until the moment of submersion, showing no indication of rising in advance of the incoming (ocean) tide. As a consequence, the water table low tide progressively delays the ocean low tide, with, in Pollock and Hummon (1971) data, a maximum delay of about 5 h just seaward of the spring high-tide position. A falling water table until submersion by the rising tide is also apparent in Raubenheimer *et al.* (1999)'s data (their Figure 4, $x = 4$ m) collected on a 1:30 sloping, medium-sand ($230 \mu\text{m}$) planar beach. On fine-grained, low-sloping beaches that experience a substantial tidal range, the water table may outcrop the beach well above the swash zone during falling tide (e.g., Turner, 1993), forming a seepage face between the outcrop location and the swash zone. Here, the water table remains at the beach surface.

Tide-induced water table fluctuations in a sandy homogeneous beach (shallow unconfined aquifer) can be predicted accurately with models based on the nonlinear Boussinesq equation (e.g., Nielsen, 1990; Baird *et al.*, 1998; Raubenheimer *et al.*, 1999). Wave set-up is commonly included at the seaward boundary and improves predictions of the overheight, particularly when wave activity is substantial (Turner *et al.*, 1997; Baird *et al.*, 1998). Wave run-up effects are generally ignored (Horn, 2002) and the run-up extension to the Boussinesq equation proposed by Nielsen *et al.* (1998) and Kang *et al.* (1994) remains largely untested. As proposed conceptually in Namikas *et al.* (2010), predictions of surface moisture content can be made with knowledge of the soil–water retention curve, which describes the moisture content as a function of height above the water table. Data collected on two non-tidal, fine-grained ($200 \mu\text{m}$) beaches (Darke

and McKenna Neuman, 2008) indeed show a dependence of surface moisture on water table depth, as expected from a retention curve, with saturated sand for $h < 0.2$ m, a drop in w_s to near 0% with an increase in h to 0.4–0.5 m and $w_s \approx 0\%$ for $h > 0.5$ m. On tidal beaches the dependence may be more complicated. Here, hysteresis effects with higher surface moisture content with falling than rising tide for the same water table depth may be substantial. This was illustrated from laboratory experiments with a vertical sand ($130 \mu\text{m}$) column and an oscillating water table (Schmutz and Namikas, 2013) and from field measurements on an upper beach (also $130 \mu\text{m}$; Padre Island National Seashore, USA) under spring tidal conditions when the groundwater depth was less than about 1 m (Schmutz, 2014). It is likely that the importance of hysteresis to surface moisture variability diminishes with increasing grain size (e.g., Yang *et al.*, 2004; Gallage and Uchimura, 2010).

The aim of this paper is to document and model cross-shore changes in tide-induced groundwater fluctuations and the associated surface-moisture dynamics on a planar, medium-grained beach. The observations stem from a 10-day dataset of water table depths and surface moisture values collected at eight cross-shore locations on a 1:30 sloping, intertidal and upper beach ($365 \mu\text{m}$) near The Hague, The Netherlands. The model is based on the nonlinear Boussinesq equation, extended with wave run-up infiltration as proposed by Nielsen *et al.* (1998), and the Van Genuchten (1980) soil–water retention curve ignoring hysteresis effects. Modelled water table water fluctuations are controlled by two free parameters (hydraulic conductivity and a run-up infiltration coefficient), and the retention curve is determined by two free shape parameters. All parameter values are obtained with data-model fitting. The relative importance of tide and wave effects to the observed groundwater fluctuations and the implications of our results for the availability of sand on the intertidal beach for aeolian transport are discussed. We finalize this paper with our main conclusions.

Methodology

Observations

Field data were collected on the western side of the Sand Engine (Netherlands; Figure 1; see also De Schipper *et al.*, 2016) in September and October 2014 as part of the international Mega-Perturbation field experiment (MegaPex). The Sand Engine is a 17 Mm^3 nourishment located near The Hague, close to the southern end of the approximately 120 km long, roughly north–south oriented Holland coast. The yearly averaged offshore significant wave height is 1.3 m. Waves are generally incident from either the southwest or northwest. The tide is semi-diurnal with a typical range of 1.4 m during neap tide, increasing to 1.8 m during spring tide. The tidal curve is distinctly asymmetric, with a more rapid rise than fall. Storms from the northwest can increase the offshore significant wave height to over 5 m, and result in a surge in excess of 1 m.

Water-level fluctuations were measured from 11 to 20 October with eight pressure transducers, each located in a well and set to store a single instantaneous value every 10 min. The wells were deployed in a cross-shore array (Figure 2) extending from just landward of the mean low-water line to above the spring high-water line, and are termed W1–W8 from sea to land. The positioning of the wells implies that the observed water level is the seawater elevation ζ when the well is submerged by the tide and the water table elevation η otherwise. The wells consisted of a steel tube of 2–4 m in length and 0.05 m in diameter, with a perforated lower end of approxi-



Figure 1. Photograph of the Sand Engine, taken on 13 September 2014 (i.e., at the start of MegaPex) in the northern direction. The black line indicates the approximate location of the instrument array. Photographer: Rijkswaterstaat/Joop van Houdt. [Colour figure can be viewed at wileyonlinelibrary.com]

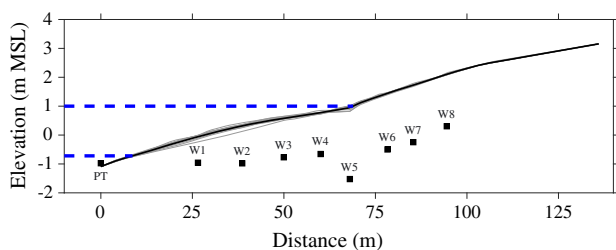


Figure 2. Elevation z with respect to mean sea level (MSL) versus cross-shore distance x . The grey lines are the profiles surveyed during the measurement period (11–20 October, 2014), and the black line is the temporal mean profile used in the groundwater modelling. The blue dashed lines indicate the mean high and low tide level. The squares are the instrument locations. The cross-shore distance is 0 at the most seaward pressure transducer (PT) and is positive onshore. [Colour figure can be viewed at wileyonlinelibrary.com]

mately 1 m. In the steel tube a PVC pipe was inserted, with a filter of $50\ \mu\text{m}$ at the lower end, to prevent the entry of sand. The height of the top of each well relative to Dutch Ordnance Datum (NAP; 0 m NAP is equal to mean sea level, MSL) was determined several times with real-time kinematic (RTK) GPS, and the individual heights were averaged. As the pressure transducers were at a known distance beneath the top of the well, the water-level fluctuations are given with respect to MSL in the following. Initial inspection of the data revealed some sample-to-sample fluctuations of 0.05–0.1 m when a well was submerged by the tide. These fluctuations are presumably wave induced and were removed by filtering each series with a quadratic loess interpolator (Plant *et al.*, 2002) with a scale λ_t of 1 h. This interpolator acts as low-pass filter and removes variability at temporal scales of $\lambda_t/0.7$ (here, ≈ 1.4 h). Visual inspection of the data revealed that this setting was effective in removing rapid fluctuations while retaining the tidal signal.

An additional pressure transducer, termed PT, was deployed 26.5 m seaward of W1 at about 0.1 m above the bed. This transducer, which was seaward of the spring low-water line and was therefore always submerged, was operational since the start of MegaPex (15 September) and sampled continuously at 10 Hz. Its data were processed in 10 min averaged values (with respect to MSL), where each block of 10 min was centred around the sample moments of the other transducers. From the time series of water-level fluctuations observed at W1–W8 the time delay of each low and high tide was deter-

mined relative to the moment of low and high tide recorded at the PT. The asymmetry (A_s) of each tidal cycle was computed at all locations as the ratio of the duration of falling tide to the total duration of the tidal cycle, taken as the time difference between two consecutive high tides, minus 0.5. In this way, A_s equals 0 for a sinusoidal tidal cycle and increases to a maximum of 0.5 when the rising tide shortens to 0. To estimate the amplitude a of a tidal cycle, the water-level time series at each location was first converted into tidal perturbations by subtracting the zero-frequency signal estimated by applying three low-pass filters (two with a width of 24 h, one with a width of 25 h; Godin, 1972). The amplitude was then taken as half the elevation difference between a high and preceding low tide.

Surface moisture content w_s was measured with a Delta-T Theta probe (e.g., Tsegaye *et al.*, 2004; Schmutz and Namikas, 2011) next to each non-submerged well on most days for 6–8 consecutive hours with a 15–30 min interval, depending on the length of the array that could be sampled. The probe measures the dielectric constant of the sand, which depends on sand properties and moisture content. Thus, if the sand properties are time invariant (as is the case here), the probe's output is related to moisture content. The probe contains four stainless steel rods that are inserted into the sand, where the probe generates and transmits a 100 MHz signal. The difference in impedance between the rods and the sand results in a reflection of this signal. Usually, the probe has rods that are 0.06 m long, but the resulting output is not necessarily representative of the moisture content at the surface. Therefore, 0.02-m long rods were used. This approach differs from earlier Delta-T Theta probe applications, in which the effective measurement length of the 0.06 m long pins was shortened with dielectric foam blocks (e.g., Yang and Davidson-Arnott, 2005; Namikas *et al.*, 2010; Schmutz and Namikas, 2011). The probe's output was calibrated using 0.02 m high sand cores from which the moisture content was determined using the standard gravimetric method. The dependence of the output of the probe used on 11 and 12 October was linearly related to moisture content, with a correlation coefficient squared r^2 of 0.96 and a standard error s_E of 1.6%. Because of technical issues this probe had to be replaced by another probe on 13 October. Its calibration curve was a third-order polynomial, with $r^2 = 0.97$ and $s_E = 1.2\%$. These statistics are similar to those reported in earlier studies (e.g., Schmutz and Namikas, 2011; Edwards *et al.*, 2013). Both calibration curves covered the full w_s range from dry ($w_s < 4\%$) to fully saturated ($w_s \approx 25\%$) sand. During the measurements the probe was inserted into the sand next to a well five times, and the recordings were then averaged, with the average converted to w_s .

Between 11 and 20 October the offshore significant wave height H_{m0} varied between 0.5 and 2.5 m (Figure 3a), and the tidal range decreased from spring to neap tide conditions (Figure 3b). The wave data were collected at the Europlatform, which is 63 km to the west of the study site in 32 m depth. The (offshore) water-level signal ζ_0 was taken as the time series of the 10 min average ζ values computed from the PT data. Beach profiles determined almost daily with an RTK-GPS illustrated that morphological change was only small (Figure 2) during the measurement period and that the beach was essentially planar with a slope of about 1:30. Only during the first few days was a subdued bar feature present in the intertidal zone, which is a remnant of a much more pronounced bar that was present during the earlier stages of MegaPex (Figure 1). Figure 3c illustrates that W1–W5 were submerged during almost all high tides, and W6 during spring high tides only. The time-varying shoreline x_{sh} shown in this panel was computed as the intersection of ζ_0 plus the breaking-wave induced set-up (see Eq. (3) below) with the time-averaged beach profile. W7

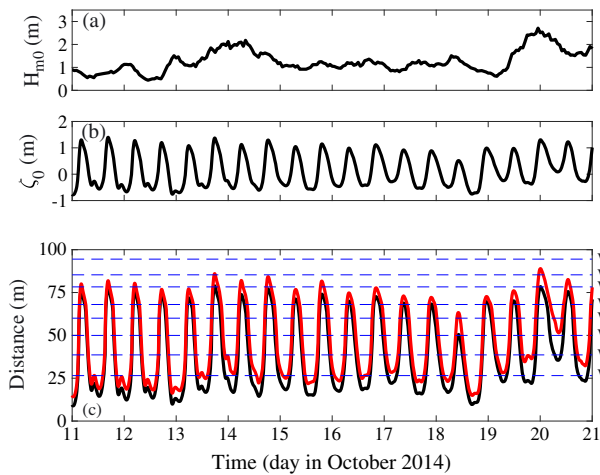


Figure 3. Time series of (a) offshore significant wave height H_{m0} , (b) offshore water level ζ_0 and (c) estimated shoreline (black line) and run-up limit (red line). In (c) the blue dashed lines are the position of the eight wells; the cross-shore distance is 0 at the most seaward pressure transducer (PT) and is positive onshore. [Colour figure can be viewed at wileyonlinelibrary.com]

and W8 were always above the estimated high-tide shoreline, but may have experienced swash/backwash activity during the days with the highest waves (e.g., 14 and 20 October). Here, the set-up and swash limit were estimated following Stockdon *et al.* (2006). The median grain size of the surface sand was about $365 \mu\text{m}$. Boreholes taken at several locations at the Sand Engine show a sandy clay layer at about 7 m below MSL, which acts as an aquitard (Huizer *et al.*, 2018). This implies that the thickness of the phreatic aquifer at the location of the wells is about 7 m.

Meteorological data during the measurement period, shown in Figure 4, were retrieved from the recordings of the Valkenburg station, which is operated by Royal Netherlands Meteorological Institute some 20 km to the north of the Sand Engine on a flat grass surface just landward of the dunes. As can be seen in Figure 4a, hourly mean wind speeds (at 10 m above ground level) were generally below 8 m s^{-1} , except on 19 October when wind speeds were up to 12 m s^{-1} . Winds blew mostly onshore from the south (180° N) to west (270° N), but offshore from the east on 12 October (Figure 4b). Air temperature (at 1.5 m above ground level) followed a diurnal pattern, with most maximum day-time temperatures near 15°C , peaking at 20°C on 18 October (Figure 4c). The sky had mostly broken cloud (5–7 oktas) or was completely overcast (8 oktas) during day-time (Figure 4d); only on 18 October were there few clouds (2 oktas or less). Despite the generally clouded conditions, precipitation was limited (Figure 4d), and never occurred during our surface-moisture sampling. Daily reference crop evaporation (Figure 4f), estimated with the Makkink equation (e.g., De Bruin and Lablans, 1998), was generally low: less than about 1.5 mm per day. It is likely that the actual evaporation from the beach was even less because of the strong limiting effect of unsaturated sand on evaporation (e.g., Wilson *et al.*, 1997; Aydin *et al.*, 2005). On the whole, it is safe to assume that precipitation and evaporation had little (if any) effect on surface moisture variability during our measurements. We return to this assumption in the Discussion.

Model

Cross-shore and temporal water table fluctuations were simulated with the commonly used nonlinear Boussinesq equation

(e.g., Raubenheimer *et al.*, 1999) with spatially constant aquifer thickness D , extended to include run-up infiltration (Nielsen *et al.*, 1998; Kang *et al.*, 1994):

$$\frac{\partial \eta'(x, t)}{\partial t} = \frac{K}{n_e} \frac{\partial}{\partial x} \left\{ [D + \eta'(x, t)] \frac{\partial \eta'(x, t)}{\partial x} \right\} + \frac{U_I}{n_e} \quad (1)$$

Here, the prime indicates a predicted value, x is cross-shore location, t is time, K is the hydraulic conductivity of the sand, n_e is the (non-dimensional) specific yield and U_I is the run-up infiltration flow rate per unit area. The Boussinesq equation follows from the substitution of Darcy's law into the continuity equation (e.g., Nielsen, 1990) and assumes that the sand is homogeneous and isotropic, and that groundwater flow is essentially horizontal. These are generally realistic assumptions for sandy beaches (e.g., Raubenheimer *et al.*, 1999). Following Nielsen *et al.* (1998), we schematize U_I as

$$U_I = \begin{cases} C_I K f(x) & \text{if } x_{cf} \leq x \leq x_{ru} \\ 0 & \text{otherwise} \end{cases} \quad (2)$$

where C_I is non-dimensional infiltration coefficient and $f(x)$ is a non-dimensional function of x . Infiltration has been observed to depend positively on the depth to the water table (Heiss *et al.*, 2014). Therefore, we take $f(x)$ to increase linearly from 0 at the location x_{cf} , where the depth of the water table equals the thickness of the capillary fringe to 1 at the maximum run-up location x_{ru} . For the sand characteristics at the Sand Engine field site we expect the thickness of the capillary fringe to be 0.2 m (Turner and Nielsen, 1997, their Figure 7) and to compute x_{ru} we use the Stockdon *et al.* (2006) parametrization. The relevance of run-up infiltration to the observed water table fluctuations is explored in the Discussion.

Equation (1) was solved numerically with a centred finite difference method in space and a fourth-order Runge–Kutta integration technique in time. The seaward boundary condition was a moving shoreline at location $x_{sh}(t)$ (see Figure 3c) with elevation $\eta'_{sh}(x_s, t)$, here taken as

$$\eta'_{sh}(x_{sh}, t) = \zeta_0(t) + \xi'_{sh}(t), \quad (3)$$

where $\xi'_{sh}(t)$ is the breaking-induced set-up at the shoreline, for which, as aforementioned, we used the Stockdon *et al.* (2006) parametrization. The imposed landward boundary condition was $\partial \eta' / \partial x = 0$. The water table model was run using the time-averaged cross-shore profile (i.e., the mean of the profiles shown in Figure 2) with a spatial grid size of 0.5 m and time step of 2 s. The profile extended from $x = 0$ at the location of the PT, to $x = 136$ m, some 40 m landward of W8. Here, we expect the semi-diurnal variations in the groundwater to have dampened completely. The model was started with η'_{sh} values from the onset of the MegaPex campaign to ensure that slow variations in $\eta'(t)$ above the high-tide level were properly included at the start of the time period of interest (11 October). From the η' time series at the location of the eight wells the amplitude and asymmetry for each tidal cycle were computed using the same approach as deployed for the measurements. Clearly, there are no η' predictions when a well location is seaward of the shoreline position. To still be able to compute a' and As' values, the measured seawater elevation and timing of high tide were then used.

To predict the surface moisture content we assume that the vertical moisture profile above the water table $\eta'(x, t)$ is hydrostatic. In other words, we ignore the effect of the rising and falling of the water table on the shape of moisture profile and

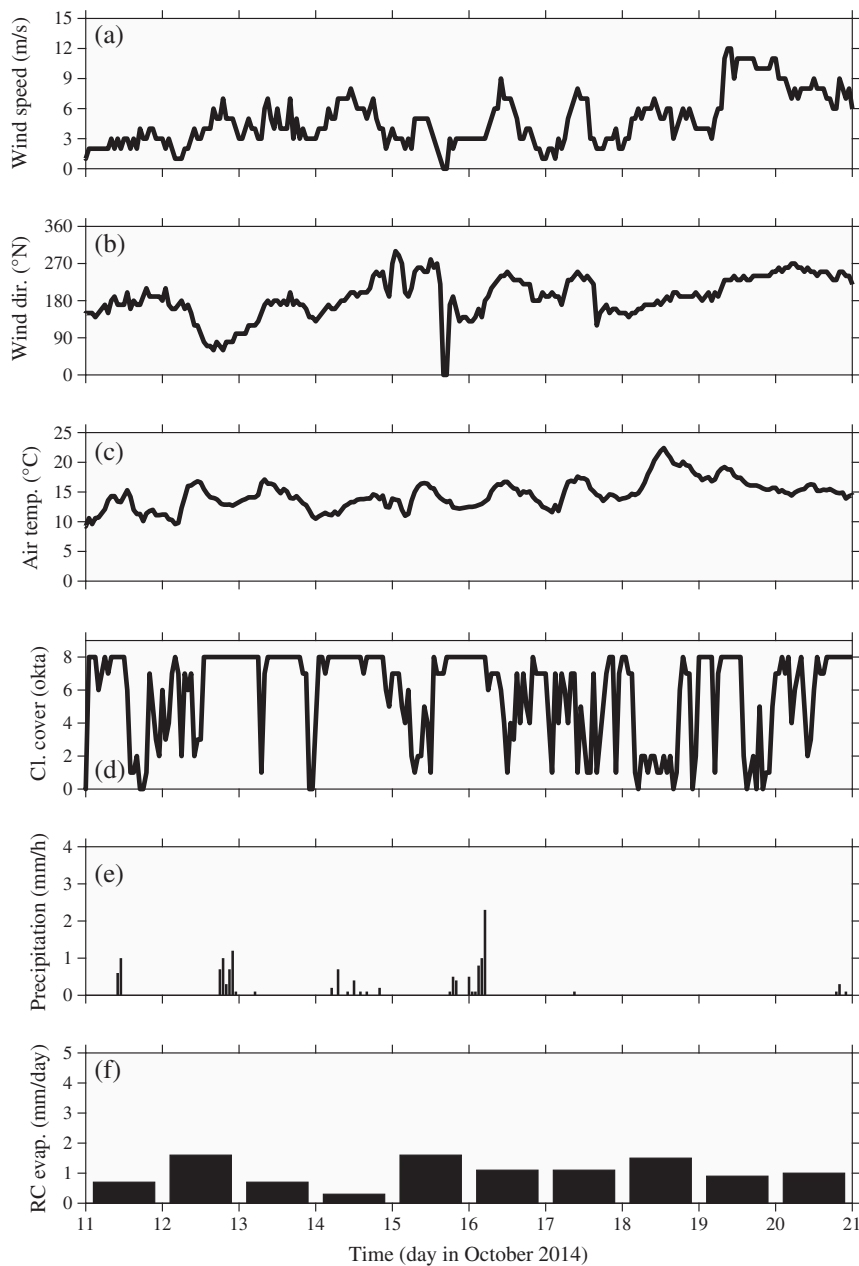


Figure 4. Time series of (a) wind speed, (b) wind direction, (c) air temperature, (d) cloud cover, (e) precipitation and (f) reference crop evaporation at station Valkenburg (about 20 km to the north of the study site) operated by the Royal Netherlands Meteorological Institute. Cloud cover is given in oktas (eighths), from completely clear (0) to overcast (8).

hence on surface moisture content, and we impose an immediate response of surface moisture content on variations in the depth of the water table. We return to the neglect of hysteresis in the Discussion. We adopted the water retention curve proposed by Van Genuchten (1980); the surface moisture content is then given by

$$w'_s(x, t) = w_{\text{res}} + \frac{w_{\text{sat}} - w_{\text{res}}}{[1 + (\alpha h(x, t))^n]^{1-1/n}} \quad (4)$$

In this equation, w_{res} and w_{sat} are the residual and saturated gravimetric water content, respectively, h is the depth of the water table beneath the bed surface, and α and n depend on the shape of the moisture profile. To illustrate our approach (see also Namikas *et al.*, 2010, and Schmutz and Namikas, 2013), Figure 5 shows predicted moisture profiles for three water table depths ($h = 1.0$ m, 0.4 m and 0.1 m), all with $w_{\text{res}} = 2\%$, $w_{\text{sat}} = 25\%$, $\alpha = 3.5 \text{ m}^{-1}$ and $n = 3.19$, where

the latter two values were based on Tuller and Or (2005). For $h = 1.0$ m (Figure 5a) the moisture profile contains an approximately 0.10–0.15 m thick capillary fringe ($w'_s \approx w_{\text{sat}}$) and a roughly 0.5 m thick layer where the moisture content gradually reduces to w_{res} . A change in slope is visible at about 0.25 m above the water table. Closer to the bed surface, the moisture content approximately equals w_{res} (in this case, $w'_s = 3.5\%$). For lower h , the surface truncates the moisture profile of Figure 5a earlier and w'_s thus increases. For the present settings, $w'_s = 11.0\%$ for $h = 0.4$ m and about equal to w_{sat} for $h = 0.1$ m because the capillary fringe now extends to the surface. We return to the values of w_{res} , w_{sat} , α and n in the Results section.

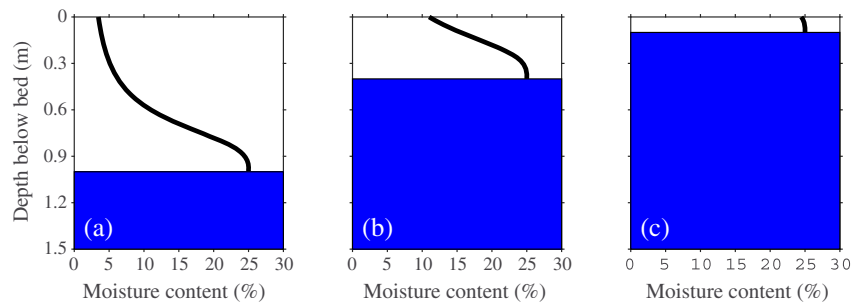


Figure 5. Predicted vertical profiles of gravimetric moisture content for three different depths h of the water table below the bed surface: (a) $h = 1.0$ m, (b) $h = 0.4$ m and (c) $h = 0.1$ m. The predictions were made with the Van Genuchten (1980) retention curve using $w_{res} = 2\%$, $w_{sat} = 25\%$, $\alpha = 3.5 \text{ m}^{-1}$ and $n = 3.19$. [Colour figure can be viewed at wileyonlinelibrary.com]

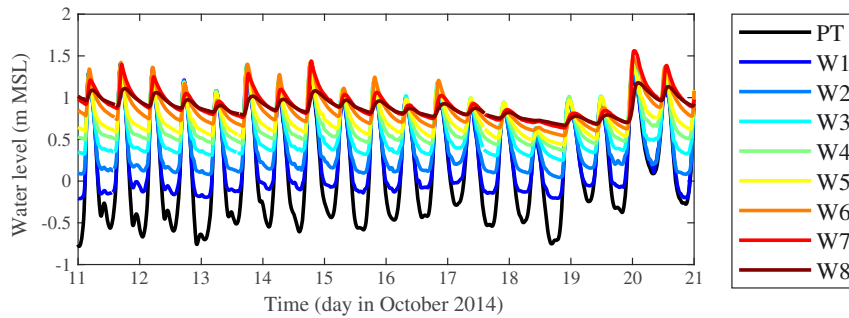


Figure 6. Time series of measured water-level fluctuations with respect to mean sea level at the eight wells and the PT. [Colour figure can be viewed at wileyonlinelibrary.com]

Results

Water table fluctuations

Measured water-level fluctuations (Figure 6) at all wells show semi-diurnal fluctuations which, consistent with earlier work (e.g., Pollock and Hummon, 1971; Lanyon *et al.*, 1982; Raubenheimer *et al.*, 1999), diminished in amplitude and changed in asymmetry in the landward direction. As can be seen in Figure 7a, the amplitude of the fluctuations normalized with that of the sea surface (PT) decreased linearly from 1 to 0.35 across the intertidal beach. In this figure cross-shore distance is normalized for each tidal cycle as $x^* = (x - x_{LT}) / (x_{HT} - x_{LT})$, in which x_{LT} and x_{HT} are the cross-shore location where a low-tide and the subsequent high-tide η'_{sh} intersect the time-mean bed profile. The intertidal beach thus corresponds to $0 \leq x^* \leq 1$. Landward of the high-tide position ($x^* > 1$) the normalized amplitude decreased further to less than 5% for $x^* > 1.5$. At each intertidal location the water table kept on falling almost until the moment the rising tide flooded it again (Figure 6). The low tide in water table fluctuations thus progressively delayed the sea-surface low tide in the direction of the high-tide position, from ≈ 0 at $x^* = 0$ to 150 min at $x^* = 1$ (Figure 7b). Because the moment of high tide at wells submerged by the sea-surface tide is equal to that determined for the PT, As increased from its tidal value (0.1–0.2 for $x^* < 0$) to peak at ≈ 0.35 at $x^* = 1$ (Figure 7c). Above the high-tide level the delay in low tide increased further to 200 min (Figure 7b). The delay in high tide quickly increased for $x^* > 1$ to almost 150 min at $x^* \approx 1.3$. As a consequence, the water table fluctuations above the high-tide location became more symmetric, with As dropping to 0.2 at $x^* \approx 1.3$ (Figure 7c). At this location the water table fluctuations were thus only weakly more asymmetric than the sea-surface tide.

The measurements landward of the high-tide position (W6 to W8 in Figure 6) illustrate a campaign-averaged overheight of approximately 0.9 m. The overheight was highest during spring tide (e.g., 11 October; Figures 6 and 8a) or high waves (e.g., 20 October; Figure 6) and lowest during neap tide with low-wave activity (e.g., 18 October; see Figures 6 and 8b). At W7 and W8 the low-pass (Godin) filtered η series dropped approximately 0.4 m from spring to neap tide, at both locations exceeding the amplitudes of the semi-diurnal tidal component. This is consistent with earlier observations that, in the case of minimal set-up, run-up and rain, groundwater fluctuations landward of the intertidal zone are predominantly driven by neap–spring variations (e.g., Turner *et al.*, 1997). The high overheight implies that the groundwater table was generally sloping seaward; only during a few hours around high tide, the water table at the shoreline exceeded the water table elevation further inland and the water table was thus sloping landward. Note from Figure 8 that the water table in the intertidal zone at low tide in ζ was closer to the bed during spring than neap tide because of the spring–neap tidal difference in the overheight. For example, at $x = 50$ m in Figure 8, the depth of the water table was 0.22 m and 0.32 m during spring and neap low tide, respectively.

With $D = 7$ m and $n_e = 0.3$, a nonlinear fit of the model predictions to the measured water table fluctuations using the Levenberg–Marquardt algorithm resulted in $K = 7.8 \times 10^{-4} \text{ m s}^{-1}$ and $C_l = 0.216$. The optimum K is close to the $K = 9.7 \times 10^{-4} \text{ m s}^{-1}$ expected from the commonly adopted Alyamani and Sen (1993) formulation with the present grain size data. A different n_e would have resulted in another optimum K , but not in different data model agreement as $\eta'(x, t)$ depends on the ratio of K to n_e (see also Baird *et al.*, 1998; Raubenheimer *et al.*, 1999). Our $C_l = 0.216$ is midway between the $C_l = 0.08$ mentioned in Kang and Nielsen (1996) for steady laboratory conditions and their $C_l = 0.45$ suggested for field conditions during rising tides. With the optimum free model

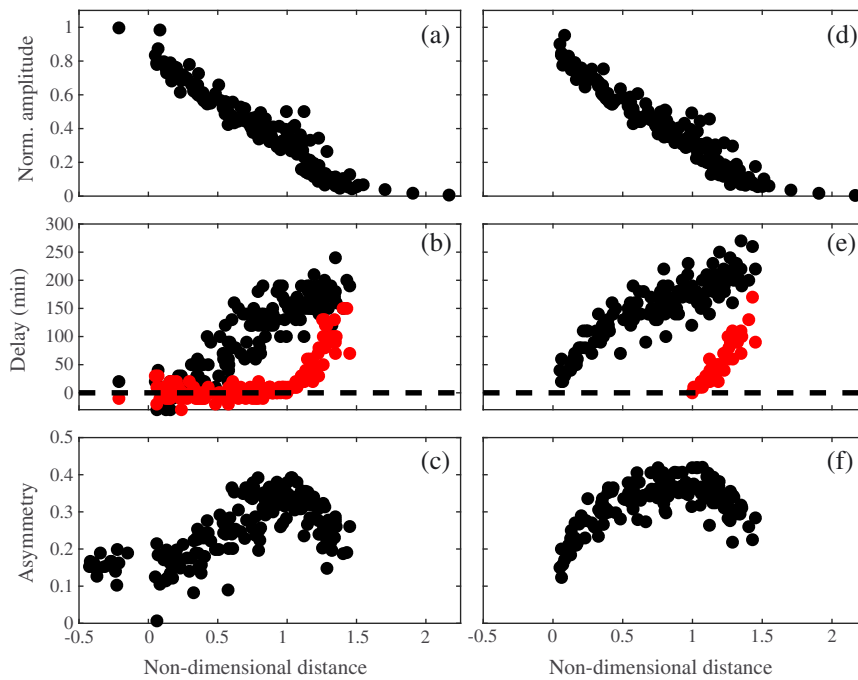


Figure 7. Measured (a) tidal amplitude a normalized with the amplitude at PT, (b) time lag with respect to the moment of (black dots) low tide and (red dots) high tide at the PT, and (c) asymmetry versus non-dimensional cross-shore distance x^* , where $x^* = 0$ and 1 correspond to the location of the low-tide and high-tide position, respectively. (d–f) are the same as (a–c) but now based on modelled water table fluctuations with $K = 7.8 \times 10^{-4} \text{ m s}^{-1}$ and $C_I = 0.216$. Values for the time lag and asymmetry are shown only when the amplitude exceeded 0.05 m. Most asymmetry values for $x^* < 0$ in (c) are based on the PT data; they are not repeated in (f). [Colour figure can be viewed at wileyonlinelibrary.com]

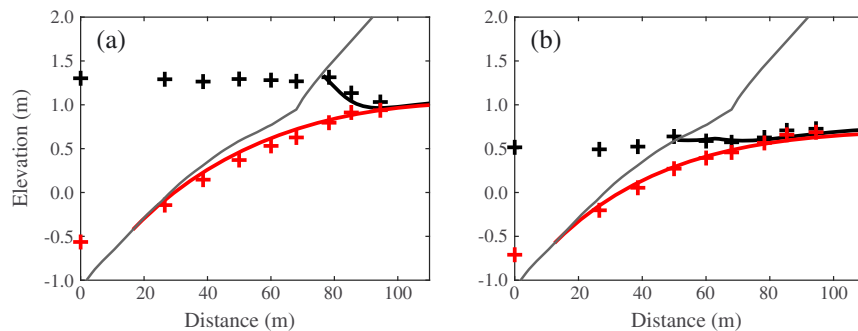


Figure 8. Measured (symbols) and modelled (thick lines) water-level fluctuations during (a) spring tide and (b) neap tide versus cross-shore distance. Black corresponds to high tide in sea-surface elevation (spring tide: 11 October, 04:10; neap tide: 18 October, 10:20), red to low tide (spring tide: 11 October, 12:30; neap tide: 18 October, 18:10). The thin black line is the campaign-averaged cross-shore bed profile. [Colour figure can be viewed at wileyonlinelibrary.com]

parameter values, the water table observations were predicted well with (absolute) bias $b \leq 0.065 \text{ m}$ and root mean square error $\epsilon_{\text{rms}} \leq 0.085 \text{ m}$ at all wells (Table I, 'Tide and waves'). As can be seen by comparing Figures 7d–7f with Figures 7a–7c, the model accurately reproduced the linear decrease in amplitude with x^* , the change in the delay of low tide and high tide across the beach, and the peak in asymmetry at $x^* \approx 1$. In more detail, the model systematically underestimated the drop in water table level below the bed at most intertidal well positions (Figures 8 and 9a), hence the positive b at W1–W5. What is more, the model predicted the water table to fall for slightly longer than in the measurements, causing the asymmetry to be slightly overestimated for $x^* < \approx 0.75$. These data model mismatches were minimal at the high-tide level (Figure 9b), as also indicated by the near-zero b and small ϵ_{rms} (0.044 m) at W6. The model accurately predicted the overheight (Figures 8b and 9c) when waves were small; otherwise (e.g., 11–12 and 20 October) the overheight was slightly underpredicted (Figures 8a and 9c). This caused the small negative b in Table I ('Tide and waves' run) at W7 and W8.

Table I. Water table model error statistics

	Tide and waves		Tide and set-up		Tide only	
	b (m)	ϵ_{rms} (m)	b (m)	ϵ_{rms} (m)	b (m)	ϵ_{rms} (m)
W1	0.038	0.056	0.036	0.054	0.030	0.051
W2	0.063	0.084	0.058	0.081	0.047	0.073
W3	0.059	0.080	0.049	0.075	0.032	0.070
W4	0.060	0.078	0.045	0.073	0.021	0.068
W5	0.053	0.068	0.033	0.063	0.001	0.067
W6	−0.007	0.044	−0.038	0.071	−0.096	0.120
W7	−0.057	0.072	−0.093	0.113	−0.142	0.167
W8	−0.021	0.040	−0.058	0.072	−0.108	0.122

Surface moisture content

Time series of surface moisture content w_s during spring (Figures 10a and 10d) and neap (Figures 11a and 11d) tide

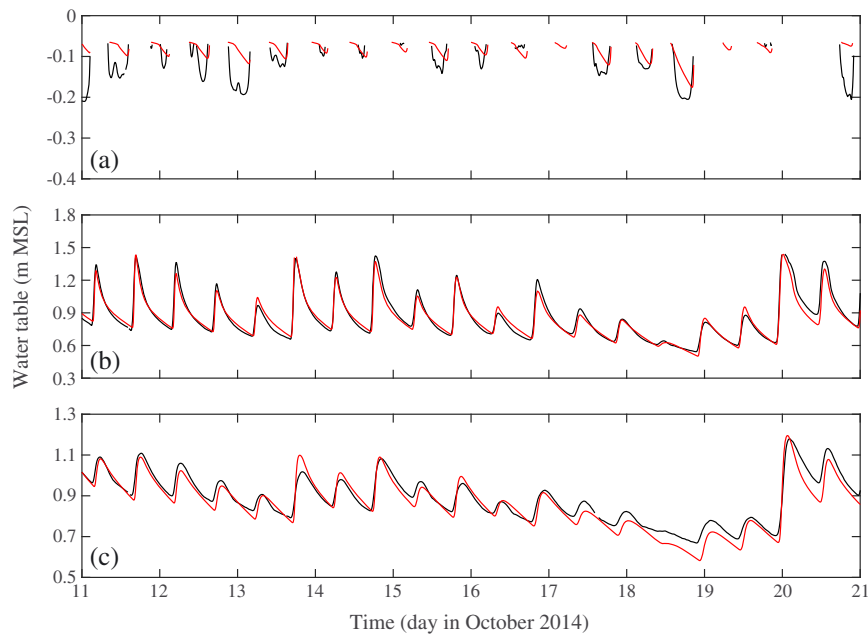


Figure 9. Time series of (black) measured and (red) modelled ($K = 7.8 \times 10^{-4} \text{ m s}^{-1}$ and $C_l = 0.216$) water table fluctuations at (a) W1, (b) W6 and (c) W8. Note the different range on the three y-axes. [Colour figure can be viewed at wileyonlinelibrary.com]

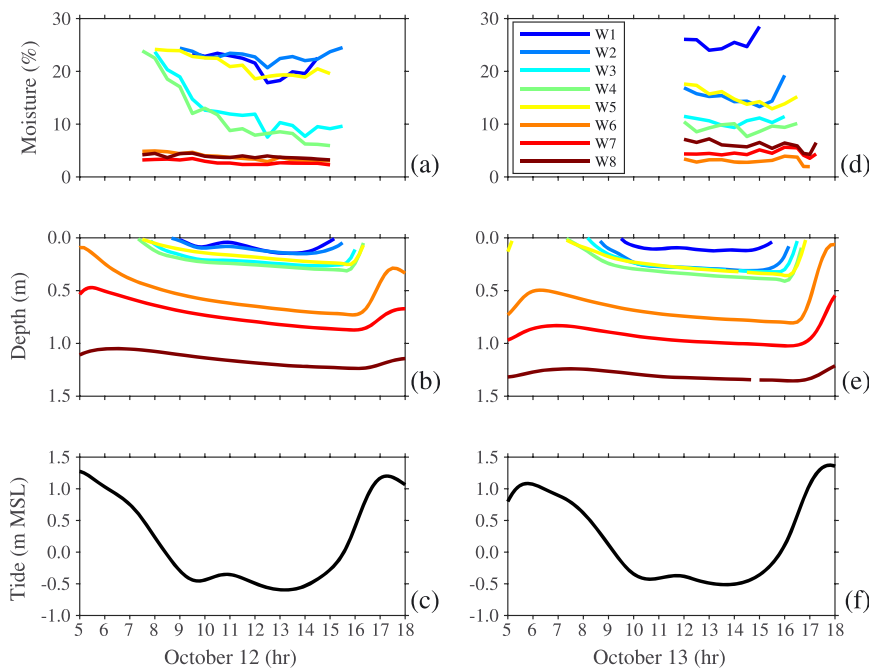


Figure 10. Time series of measured (a, d) surface moisture content w_s and (b, e) depth h of the water table beneath the bed surface at the eight wells during spring tide on 12 October (left) and 13 October (right). Panels (c, f) show sea-water elevation ζ at the PT for reference. The measurements on 12 and 13 October were conducted during falling and rising ζ , respectively, together providing a view of the spatiotemporal variability in w_s during a complete tidal cycle. [Colour figure can be viewed at wileyonlinelibrary.com]

illustrate that, consistent with Namikas *et al.* (2010), the near-planar beach at our study site can be separated into three cross-shore zones with different temporal w_s trends. Firstly, at the lower part of the intertidal beach (W1; and W2 on 12 October) w_s always exceeded about 18% (i.e., the sand was always saturated) and showed little temporal variation. This was also the case at W5 on 12 October (Figure 10a), which was on that day located in the remnant of an intertidal trough (Figure 2). Secondly, higher up on the intertidal beach (W2–W5) the beach dried with time to values of approximately 6–15%, with lower minimum values closer to the high-tide position. The decrease in w_s with time was initially

fast and then levelled off, giving the overall impression of an exponential decay with time. For example, at W5 on 16 October (Figure 11a) w_s halved from 26% to 13% during the first 2.5 h after high tide to reduce further to 9.5% only during the subsequent 2.5 h. The decrease in w_s continued even after low tide in ζ . What is more, w_s mostly decreased until inundation by the rising tide. In only a few cases (e.g., at W2 on 13 and 18 October; Figures 10d and 11d, respectively) w_s started to increase before submergence. And thirdly, the beach above the high-tide level (W6–W8) was always dry, with w_s less than 5–8% and little to no variation with time. Only on 20 October were the w_s at W6–W8 somewhat higher (6–11%; not shown).

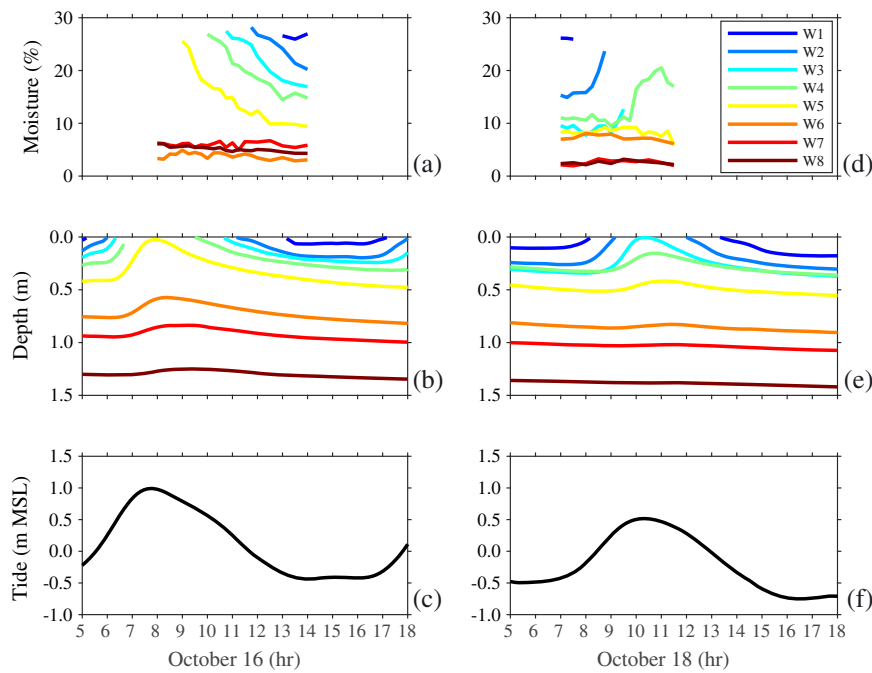


Figure 11. Time series of measured (a, d) surface moisture content w_s and (b, e) depth h of the water table beneath the bed surface at the eight wells during neap tide on 16 October (left) and 18 October (right). Panels (c, f) show sea-water elevation ζ at the PT for reference. The measurements on 16 and 18 October were conducted during falling and rising ζ , respectively, together providing a view of the spatiotemporal variability in w_s during a complete tidal cycle. [Colour figure can be viewed at wileyonlinelibrary.com]

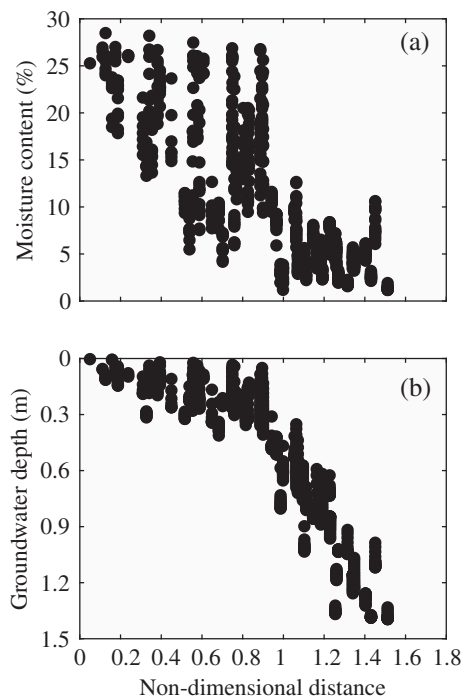


Figure 12. Measured (a) surface moisture content w_s and (b) groundwater depth h versus non-dimensional cross-shore distance, where $x^* = 0$ and 1 correspond to the location of the low-tide and high-tide position, respectively. Values in (b) are shown only when there was a corresponding moisture measurement.

Figure 12a shows that the three beach zones correspond to approximately $0 < x^* < 0.3$, $0.3 < x^* < 1$ and $x^* > 1$.

The spatiotemporal variability in w_s is controlled strongly by the depth h of the water table (compare Figures 10b and 10e with Figures 10a and 10d; Figures 11b and 11e with Figures 11a and 11d; and Figure 12b with Figure 12a). In zone

1, where the sand at the beach surface is always saturated, h was less than about 0.15–0.20 m. This corresponds to the situation where the capillary fringe extends (almost) to the beach surface, as sketched in Figure 5c. In the remnant of the intertidal trough (W5, 12 October) the water table was also close to the surface (Figure 10b), explaining the high w_s (Figure 10a). In zone 2 w_s started to decrease when the water table fell to more than 0.15–0.20 m beneath the surface to reach $\approx 6\%$ when $h = 0.4$ –0.5 m (e.g., Figure 12). The ongoing drop in w_s during the rise in ζ after low tide is due to the ongoing lowering of the water table. The temporal w_s variability in zone 2 thus corresponds to the situation sketched in Figure 5b, where the bed surface intersects the retention curve at increasingly lower w_s with increasingly larger h . As aforementioned, the reverse situation with a rising water table rarely occurred and appears to be restricted to a few moments just before submergence. In zone 3 h always exceeded 0.4–0.5 m. Apparently, the water table was too deep for its variations to affect the magnitude of w_s . Here, the measured w_s thus corresponds to the residual moisture content (Figure 5a). The higher w_s at W6–W8 on 20 October are likely related to swash events during the preceding high tide with high wave activity (Figure 3).

The shape of the dependence of surface moisture content on the depth of the water table closely resembles that expected from Equation (4), with a thickness of the capillary fringe of about 0.1–0.15 m and an inflexion point near $h = 0.2$ m (Figure 13). To find best-fit parameters for α and n , the w_s observations were first binned according to $h \pm 0.02$ m. With $w_{\text{sat}} = 25.1\%$ (the mean of the two lowermost bins) and $w_{\text{res}} = 4.2\%$ (the mean of all bins with midpoints exceeding 0.6 m) a nonlinear fit of Equation (4) to the grouped w_s yielded $n = 3.18$ and $\alpha = 5.31 \text{ m}^{-1}$. The optimum n is essentially identical to the ‘typical’ n stated in Tuller and Or (2005) for sand (3.19); the optimum α is somewhat lower (3.5 m^{-1}), implying that the present sand is somewhat better sorted than in Tuller and Or (2005)’s database and that, accordingly, the reduction from saturated to dry sand happens over a narrower range in water table depths. The r^2 of the fit amounted

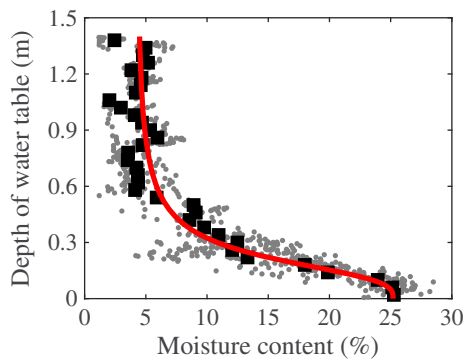


Figure 13. Measured depth h of the water table versus surface moisture content w_s . The grey dots are all individual observations, but excluding the moisture values of W6, W7 and W8 measured on 20 October. These values were higher (6–11%) than on other days, presumably because run-up reached these locations during the preceding high tide (Figure 3c) and w_s was, as a consequence, not determined by the depth of the water table. The black squares are the mean values in 0.04 m wide h classes. The red line is the best-fit Equation (4) through these grouped values, with $w_{\text{sat}} = 25.1\%$, $w_{\text{res}} = 4.3\%$, $n = 3.18$ and $\alpha = 5.31 \text{ m}^{-1}$. [Colour figure can be viewed at wileyonlinelibrary.com]

to 0.97 and the ϵ_{rms} to 1.23%. The space–time diagram of surface moisture content predicted with Equation (4) with the water table depth from the optimum Equation (1) is shown in Figure 14 and clearly displays the three cross-shore beach zones identified from the observations.

Discussion

Model assumptions

The water table model yields accurate results when including run-up infiltration (positive optimum C_I). A simulation with optimum K but without run-up infiltration ($C_I = 0$) shows an increased underprediction of the overheight, resulting in larger negative bias values for W6–W8 (Table I, ‘Tide and set-up’ run). This is consistent with Huizer *et al.* (2017) modelling study, which also shows improved skill in predicting the overheight (and temporal variability therein) in a coastal aquifer when including run-up infiltration. A further simulation without set-up and run-up shows an even more marked increase in the bias at W6–W8 (Table I, ‘Tide only’ run), suggesting that, at least for the present situation, the inclusion of set-up at the seaward boundary is more important for accurate water table predictions than the inclusion of run-up infiltration. In the intertidal zone the model performance is substantially less sensitive to C_I . This is largely due to our choices to impose run-up infiltration only when the predicted water table depth exceeds a chosen thickness of the capillary fringe and to have maximum infiltration at the landward run-up limit. This causes run-up infiltration over much of the intertidal beach to be either absent or minimal, in the latter situation with generally larger infiltration during rising than falling tide. A simulation in which we imposed run-up infiltration from the shoreline (i.e., x_{sh} rather than x_{cf} in Equation (2)) caused the water table to exit the beach well above the shoreline, thus forming the landward boundary of a seepage face. This clearly contrasts with the observations (Figures 6 and 9). There is considerable uncertainty on the functional cross-shore shape of run-up infiltration. For example, Kang *et al.* (1994) inferred $f(x)$ to be maximum roughly midway between the shoreline and the run-up limit from measured cross-shore water table fluctuation

during a single rising tide on an Australian beach, while Huizer *et al.* (2017) imposed $f(x)$ to decrease from 1 at x_{sh} to 0.1 at x_{ru} . Therefore, although Equation (2) contributes to accurate water table predictions, temporal and spatial variability in run-up infiltration may not be modelled accurately.

Our findings show that, at least at our site, a non-hysteretic approach suffices to describe the dependence of surface moisture content on water table depth. As in data from other intertidal beaches (e.g., Pollock and Hummon, 1971; Raubenheimer *et al.*, 1999), the emerged part of the Sand Engine intertidal beach essentially always experiences a falling groundwater table irrespective of whether the sea-water elevation falls or rises. This foregoes the need to have separate drying and wetting retention curves. Whether a hysteretic approach is necessary on the upper beach depends on the retention properties of the sediment. These are related to the pore characteristics, which, in turn, scale with the sediment grain size and sorting (e.g., Aubertin *et al.*, 2003). With a decrease in grain size the thickness of the capillary fringe increases, while further above the water table the moisture content will be higher in comparison to coarser sediment at the same vertical distance to the water table. The relatively coarse sand at the Sand Engine results in a fairly thin capillary fringe (0.1–0.15 m) and a change from w_{sat} to w_{res} when h increases to about 0.5 m (Figure 13). As the water table on the Sand Engine’s upper beach generally exceeds this depth, the moisture content is close to its residual value and hysteresis effects are, as a consequence, minimal. For beaches with substantially finer sands than considered here, hysteresis-based modelling will become necessary to accurately predict the temporal variability in upper-beach surface moisture content, as illustrated by Schmutz and Namikas (2013) and Schmutz (2014) for a 130 μm sand.

The overall good correspondence between w_s and h (Figure 13) and the minimal variations in w_s on the upper beach (Figures 10 and 11) imply that factors other than water table depth, such as evaporation, were not important to w_s variability. Evaporation is likely to vary substantially across the beach profile given its dependence on moisture content, with larger rates from the wetter part of the beach (cf. Wilson *et al.*, 1997; Aydin *et al.*, 2005). However, these larger evaporation values are unlikely to decrease surface moisture content, as there will be an immediate replenishment of the evaporated water by capillary rise from the high water table. Indeed, model simulations of spatial-temporal surface moisture dynamics that included both atmospheric and groundwater processes, presented in Schmutz (2014), revealed that evaporation was relevant to the accurate prediction of surface moisture dynamics on the upper beach only, where water table depth exceeded 1 m and capillary rise was hence minimal. Although evaporation may thus be a key control factor for surface moisture dynamics on the upper beach, we believe that its inclusion in our model is not necessary from an aeolian perspective: the surface moisture content here is close to w_{res} and will have little or no effect on aeolian processes (cf. Delgado-Fernandez, 2011).

Implications for aeolian transport

Although the intertidal beach has been argued to be a substantial source for wind-blown sand (e.g., De Vries *et al.*, 2014b; Hoonhout and De Vries, 2017), our data indicate that sand on the lower 50% of the Sand Engine beach is always too wet ($w_s > 10 - 15\%$) to become entrained by the wind (Figure 12a), while that on the upper 50% is sufficiently dry to become available for aeolian transport for a short period

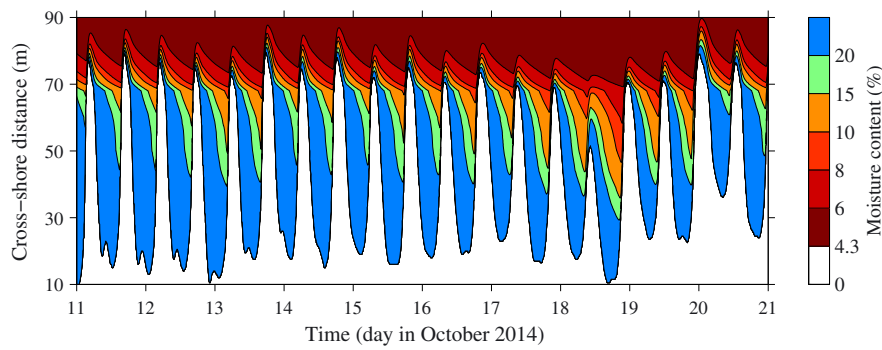


Figure 14. Space–time diagram of predicted surface moisture content w'_s based on Equations (1) and (4), both with optimum parameter values, for the study period of 11–20 October 2014. The change in the slope of the moisture contours at $x \approx 70$ m is due to the small change in the slope of the bed surface (see Figure 2). [Colour figure can be viewed at wileyonlinelibrary.com]

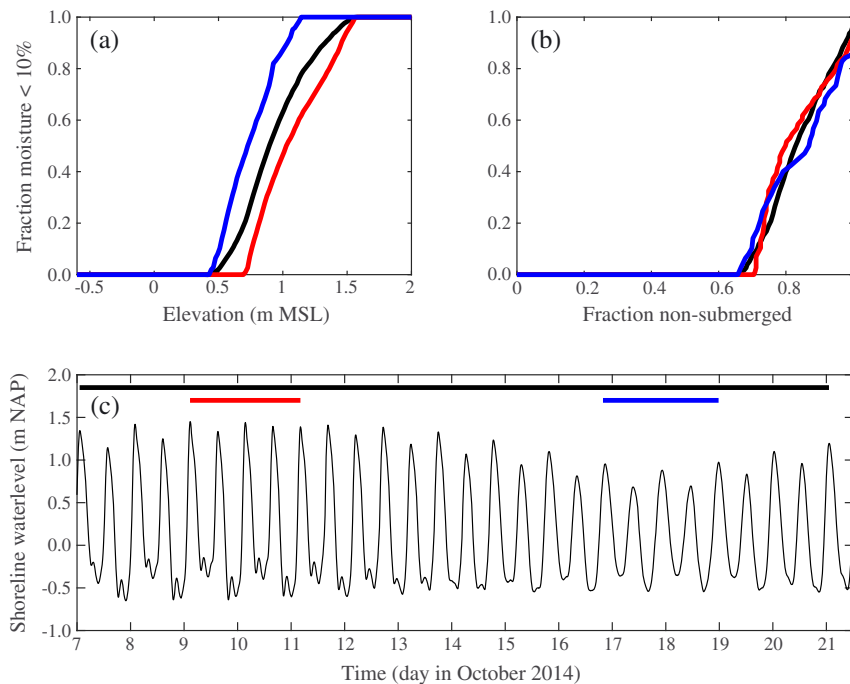


Figure 15. Fraction of time the predicted surface moisture content w'_s is less than 10% during (black) a neap–spring tidal cycle, (red) two consecutive tidal cycles during spring conditions and (blue) two consecutive tidal cycles during neap conditions (a) versus bed elevation z with respect to mean sea level and (b) fraction of time the beach is not submerged by the tide. The predictions are based on water table fluctuations driven by (c) astronomical water levels at the shoreline; the horizontal coloured lines correspond to the time period used for the computations in (a) and (b). [Colour figure can be viewed at wileyonlinelibrary.com]

of time only (e.g., Figure 11a). To examine sand availability further, a surface-moisture space–time diagram was computed for an astronomical spring–neap tidal cycle at the Sand Engine (here, 7–21 October 2014) and a 1:30 planar beach. It must be noted that at the Sand Engine spring–neap tidal variations are particularly evident in the high-water tidal levels (≈ 1.4 m MSL at spring tide and ≈ 0.9 m MSL at neap tide) but not in the low-water levels (about constant at -0.6 m MSL; Figure 15c). If $w'_s = 10\%$ is taken as the upper limit for sand availability, then only sand at bed elevations z exceeding about 0.45 m MSL can potentially become entrained in the air flow (Figure 15a, black line). This part of the beach is non-submerged by the tide for at least 66% in time (Figure 15b). Interestingly, more sand is potentially available for aeolian transport during neap than spring tide. Firstly, a larger part of the beach remains non-submerged at neap high tide, resulting in a greater area of dry sand ($z > 1.2$ m versus $z > 1.6$ m at spring tide; Figure 15a). Secondly, for $0.45 < z < 1.2$ m the fraction of time w'_s is less than 10% during neap tide well exceeds

that during spring tide. For example, at $z = 0.9$ m this fraction is estimated at 73% and 33% during neap and spring tide, respectively (Figure 15a). This difference is caused by the longer time available for drying during neap tide (Figure 15b) and, in particular, the larger overheight during spring tide. As noted from the observations (Figure 6), the latter causes the water table to drop less and hence surface moisture content to remain higher. If we had taken a higher w'_s threshold, a larger portion of the beach would obviously have become available for aeolian transport. But even for the 14% threshold mentioned in Sarre (1988), the minimum z with sufficiently dry sand is still well above 0 m MSL (≈ 0.3 m) and the spring–neap tidal differences remain.

Because our moisture measurements are depth-integrated values of the upper 2 cm of beach sand, it is possible that they are biased high (i.e., too wet) compared to actual surface values and that, as a consequence, the availability of sand for aeolian transport was underestimated in the previous paragraph. Edwards *et al.* (2013), for example, found mois-

ture content values estimated with a Delta-T probe modified with foam blocks to yield an effective 1.5 cm sampling depth to be, on average, 2.5% wetter than values determined from surface scrapings. Moisture values in the range of 5–15%, typically found on the upper intertidal beach (e.g., Figure 12a), deviated most, with negligible differences for dry and very wet sand. Despite the potential bias in our moisture observations, the model finding that sand is available for aeolian transport at bed elevations well above MSL appears to be robust, given the findings for the 10% and 14% moisture thresholds. Furthermore, Edwards *et al.* (2013) data comprised 16 samples from a fine-grained (140 μm) beach only and the generality of their findings is thus not known. A field campaign with intertidal water table wells and a near-infrared terrestrial laser scanner (e.g., Smit *et al.*, 2018) to estimate true surface moisture values could shed more precise light on the dependence of surface moisture content and water table depths.

Because of the observed strong dependence of surface moisture on the water table depth in our data and the good performance of the proposed water table–moisture model, we see it as a precursor to a quantitatively realistic aeolian sand-supply model. This will demand its coupling to, for example, the aeolian fetch model of Bauer and Davidson-Arnott (2002) or the advection model of De Vries *et al.* (2014a). However, beach–dune interaction does not involve aeolian processes only: it is also controlled strongly by marine processes and vegetation development. Low-energy, mostly long-period (swell) waves stimulate onshore sand transport (e.g., Aagaard *et al.*, 2002; Hoefel and Elgar, 2003; Brinkkemper *et al.*, 2018) and can result in the welding ashore of sandbars. This, in turn, results in a major new source of sand that potentially becomes available for aeolian transport (e.g., Houser, 2009). In contrast, higher-energy storm waves generally erode the beach and, if the water levels are sufficiently high, the foredune as well. To simulate the evolution of the entire nearshore–beach–dune system the envisaged aeolian sand-supply model has to be coupled to a model for coastal evolution in response to wave processes, such as XBeach (Roelvink *et al.*, 2009). To specifically consider dune growth, an extension with a vegetation-development model is necessary too (e.g., Keijsers *et al.*, 2016). Although promising model-coupling developments have recently been proposed in Cohn (2018), we believe that our understanding of aeolian and shallow-water marine processes, and of sand–vegetation interaction, needs to be improved substantially before such a coupled aeolian–marine–vegetation model can be used to accurately simulate beach–dune co-evolution, especially on timescales of months or longer.

Conclusions

Observations on an approximately planar (1:30), medium-grained (365 μm) beach show water table depth to be the main driver of spatiotemporal surface moisture content. On the intertidal beach the water table falls from the moment of emersion of the bed surface during falling tide to the moment of its submersion by the incoming tide. As soon as the water table is more than 0.1–0.2 m beneath the bed, the surface moisture content starts to reduce with time, with an approximate 50% reduction in about 2.5 h. The decrease in w_s with time is initially fast and then levels off. For shallower water tables, the bed surface intersects the capillary fringe above the water table and the sand remains saturated ($w_s \approx 20\%$). The observations indicate that this is the case for the lower 30% of the intertidal beach at our study site. Above the high-tide level the water table is always deeper than 0.5

m and, as a result, the moisture content is low ($w_s < 5 - 8\%$) and time invariant. The observed dependence of surface moisture content on water table depth is predicted well ($r^2 = 0.97$) from the soil–water retention curve proposed by Van Genuchten (1980) without hysteresis (wetting and drying) effects. We coupled this curve to the nonlinear Boussinesq equation, which, consistent with earlier work, predicted the observed spatial and temporal water table fluctuations well, to yield a predictive model for spatiotemporal surface moisture variability. An application of the water table–moisture model to a neap–spring tidal cycle on a 1:30 sloping beach suggests that only the intertidal beach well above mean sea level may dry sufficiently for sand to become available for aeolian transport. We see the model as a precursor to a quantitatively realistic aeolian sand-supply model and, when coupled to models predicting wave processes and vegetation development, to a model to simulate the evolution of the entire nearshore–beach–dune system.

Acknowledgements— We are greatly indebted to Florian van der Steen, Marieke Dirksen, Anouk de Bakker, Jantien Rutten and Joost Brinkkemper for their help in collecting the data, and to Chris Roosendaal, Marcel van Maarseveen and Henk Markies for excellent technical support. We thank the NatureCoast and NEMO teams for organizing the MegaPex field campaign and for providing logistical support. We are grateful to an anonymous reviewer and the associate editor for constructive comments and suggestions. All measured groundwater levels, surface moisture contents, bed profiles and PT water levels used in this publication are hosted on the Zenodo repository (doi:10.5281/zenodo.1298526). The offshore wave data are publicly available from Rijkswaterstaat (waterinfo.rws.nl) and the meteorological conditions from the climatology database of the Royal Netherlands Meteorological Institute (https://waterinfo.rws.nl). The MATLAB® code of the water table–moisture model is hosted on the GitHub site of the Utrecht Coastal Research Group (https://github.com/UtrechtCoastalGroup/Aeolus). The research presented here was funded by the Dutch Technology Foundation (STW) of the Netherlands Organisation for Scientific Research (NWO), Vici project #13709 to GR and Perspectief project NatureCoast, S1-Coastal Safety, #12686. The authors declare no conflict of interest.

References

- Aagaard T, Black KP, Greenwood B. 2002. Cross-shore suspended sediment transport in the surf zone: a field-based parameterization. *Marine Geology* **185**: 283–302.
- Alyamani MS, Sen Z. 1993. Determination of hydraulic conductivity from complete grain-size distribution curves. *Groundwater* **31**: 551–555.
- Atherton RJ, Baird AJ, Wiggs GFS. 2001. Inter-tidal dynamics of surface moisture content on a meso-tidal beach. *Journal of Coastal Research* **17**: 482–489.
- Aubertin M, Mbonimpa M, Bussi re B, Chapuis RP. 2003. A model to predict the water retention curve from basic geotechnical properties. *Canadian Geotechnical Journal* **40**: 1104–1122.
- Aydin M, Yang SL, Kurt N, Yano T. 2005. Test of a simple model for estimating evaporation from bare soils in different environments. *Ecological Modelling* **182**: 91–105.
- Baird AJ, Mason T, Horn DP. 1998. Validation of a Boussinesq model of beach ground water behaviour. *Marine Geology* **148**: 55–69.
- Bauer BO, Davidson-Arnott RGD. 2002. A general framework for modeling sediment supply to coastal dunes including wind angle, beach geometry, and fetch effects. *Geomorphology* **49**: 89–108.
- Bauer BO, Davidson-Arnott RGD, Hesp PA, Namikas SL, Ollerhead J, Walker IJ. 2009. Aeolian sediment transport on a beach: surface moisture, wind fetch, and mean transport. *Geomorphology* **105**: 106–116.
- Brinkkemper JA, Aagaard T, de Bakker ATM, Ruessink BG. 2018. Short-wave sand transport in the shallow surf zone. *Journal of Geophysical Research: Earth Surface* **123**: 1145–1159.

- Cohn N. 2018. *From the shoreface to the foredunes: coastal morphodynamics across the land–sea interface*. PhD dissertation, Oregon State University, Corvallis, OR.
- Darke I, McKenna Neuman C. 2008. Field study of beach water content as a guide to wind erosion potential. *Journal of Coastal Research* **24**: 1200–1208.
- Davidson Arnott RGD, Yang Y, Ollerhead J, Hesp PA, Walker IJ. 2008. The effects of surface moisture on aeolian sediment transport threshold and mass flux on a beach. *Earth Surface Processes and Landforms* **33**: 55–74.
- Davidson-Arnott RGD, Law MN. 1996. Measurements and prediction of long-term sediment supply to coastal foredunes. *Journal of Coastal Research* **12**: 654–663.
- De Bruin HAR, Lablans WN. 1998. Reference crop evapotranspiration determined with a modified Makkink equation. *Hydrological Processes* **12**: 1053–1062.
- De Schipper MA, De Vries S, Ruessink G, De Zeeuw RC, Rutten J, Van Gelder-Maas C, Stive MJF. 2016. Initial spreading of a mega feeder nourishment: observations of the Sand Engine pilot project. *Coastal Engineering* **111**: 23–38.
- De Vries S, Arens SM, De Schipper MA, Ranasinghe R. 2014b. Aeolian sediment transport on a beach with varying sediment supply. *Aeolian Research* **15**: 235–244.
- De Vries S, Southgate HN, Kanning W, Ranasinghe R. 2012. Dune behavior and aeolian transport on decadal timescales. *Coastal Engineering* **67**: 41–53.
- De Vries S, Van Thiel de Vries JSM, Van Rijn LC, Arens SM, Ranasinghe R. 2014a. Aeolian sediment transport in supply limited situations. *Aeolian Research* **12**: 75–85.
- Delgado-Fernandez I. 2010. A review of the application of the fetch effect to modelling sand supply to coastal foredunes. *Aeolian Research* **2**: 61–70.
- Delgado-Fernandez I. 2011. Meso-scale modelling of aeolian sediment input to coastal dunes. *Geomorphology* **130**: 230–243.
- Edwards BL, Schmutz PP, Namikas SL. 2013. Comparison of surface moisture measurements with depth-integrated moisture measurements on a fine-grained beach. *Journal of Coastal Research* **29**: 1284–1291.
- Gallage CPK, Uchimura T. 2010. Effects of dry density and grain size distribution on soil-water characteristic curves of sandy soil. *Soils and Foundations* **50**: 161–172.
- Godin G. 1972. *The Analysis of Tides*. Liverpool University Press: Liverpool, UK.
- Heiss J W, Ullman W J, Michael H A. 2014. Swash zone moisture dynamics and unsaturated infiltration in two sandy beach aquifers. *Estuarine, Coastal and Shelf Science* **143**: 20–31.
- Hoefel F, Elgar S. 2003. Wave-induced sediment transport and sand-bar migration. *Science* **299**: 1885–1887.
- Hoonhout BM, De Vries S. 2016. A process-based model for aeolian sediment transport and spatiotemporal varying sediment availability. *Journal of Geophysical Research: Earth Surface* **121**: 1555–1575.
- Hoonhout B, De Vries S. 2017. Field measurements on spatial variations in aeolian sediment availability at the Sand Motor mega nourishment. *Aeolian Research* **24**: 93–104.
- Horn DP. 2002. Beach groundwater dynamics. *Geomorphology* **48**: 121–146.
- Houser C. 2009. Synchronization of transport and supply in beach–dune interaction. *Progress in Physical Geography* **33**: 733–746.
- Huisman CE, Bryan KR, Coco G, Ruessink BG. 2011. The use of video imagery to analyse groundwater and shoreline dynamics on a dissipative beach. *Continental Shelf Research* **31**: 1728–1738.
- Huizer S, Karaoulis MC, Oude Essink GHP, Bierkens MFP. 2017. Monitoring and simulation of salinity changes in response to tide and storm surges in a sandy coastal aquifer system. *Water Resources Research* **53**: 6487–6509. <https://doi.org/10.1002/2016WR020339>.
- Huizer S, Radermacher M, De Vries S, Oude Essink GHP, Bierkens MFP. 2018. Impact of coastal forcing and groundwater recharge on the growth of fresh groundwater resources in a mega-scale beach nourishment. *Hydrology and Earth System Sciences* **22**: 1065–1080.
- Jackson NL, Nordstrom KF. 1997. Effects of time-dependent moisture content of surface sediments on aeolian transport rates across a beach, Wilwood, New Jersey, USA. *Earth Surface Processes and Landforms* **22**: 611–621.
- Kang HY, Nielsen P. 1996. *Water table dynamics in coastal areas*. In Proceedings of the 25th International Conference on Coastal Engineering: Orlando, FL, USA, 4601–4612.
- Kang HY, Nielsen P, Hanslow DJ. 1994. *Watertable overheight due to wave runup on a sandy beach*. In Proceedings of the 24th International Conference on Coastal Engineering: Kobe, Japan, 2115–2124.
- Keijsers JGS, de Groot AV, Riksen MJPM. 2016. Modeling the biogeomorphic evolution of coastal dunes in response to climate change. *Journal of Geophysical Research: Earth Surface* **121**: 1161–1181.
- Keijsers JGS, Poortinga A, Riksen MJPM, Maroulis J. 2014. Spatio-temporal variability in accretion and erosion of coastal foredunes in the Netherlands: regional climate and local topography. *PLOS ONE* **9**: e91115. <https://doi.org/10.1371/journal.pone.0091115>.
- Lanyon JA, Eliot IG, Clarke DJ. 1982. Groundwater-level variation during semidiurnal spring tidal cycles on a sandy beach. *Australian Journal of Marine and Freshwater Research* **33**: 377–400.
- Namikas SL, Edwards BL, Bitton MCA, Booth JL, Zhu Y. 2010. Temporal and spatial variabilities in the surface moisture content of a fine-grained beach. *Geomorphology* **114**: 303–310.
- Namikas SL, Sherman DJ. 1995. A review of the effects of surface moisture content on aeolian sand transport. In *Desert Aeolian Processes*, Tchakerian VP (ed), Chapman & Hall: London; 269–293.
- Nield JM, Wiggs GFS, Squirrel RS. 2011. Aeolian sand strip mobility and protodune development on a drying beach: examining surface moisture and surface roughness patterns measured by terrestrial laser scanning. *Earth Surface Processes and Landforms* **36**: 513–522.
- Nielsen P. 1990. Tidal dynamics of the water table in beaches. *Water Resources Research* **26**: 2127–2134.
- Nielsen P, Davis GA, Winterbourne J, Elias G. Wave setup and the watertable in sandy beaches, Technical Report Technical Memorandum 88/1, New South Wales Public Works Department Coastal Branch, 1998.
- Oblinger A, Anthony EJ. 2008. Surface moisture variation on a multi-barred macrotidal beach: implications for aeolian sand transport. *Journal of Coastal Research* **24**: 1194–1199.
- Plant NG, Holland KT, Puleo JA. 2002. Analysis of the scale of errors in nearshore bathymetric data. *Marine Geology* **191**: 71–86.
- Pollock LW, Hummon WD. 1971. Cyclic changes in interstitial water content, atmospheric exposure, and temperature in a marine beach. *Limnology and Oceanography* **16**: 522–535.
- Poortinga A, van Rheenen H, Ellis JT, Sherman DJ. 2015. Measuring aeolian sand transport using acoustic sensors. *Aeolian Research* **16**: 143–151.
- Raubenheimer B, Guza R T, Elgar S. 1999. Tidal water table fluctuations in a sandy ocean beach. *Water Resources Research* **35**: 2313–2320.
- Roelvink D, Reniers A, van Dongeren A, van Thiel de Vries J, McCall R, Lescinski J. 2009. Modelling storm impacts on beaches, dunes and barrier islands. *Coastal Engineering* **56**: 1133–1152.
- Salvat B. 1964. Les conditions hydrodynamiques interstitielles des sédiments meubles intertidaux et al répartition verticale de la faune endogée. *Comptes Rendus Hebdomadaires des Séances de l'Académie des Sciences* **259**: 1576–1579.
- Sarre RD. 1988. Evaluation of aeolian sand transport equations using intertidal zone measurements, Saunton Sands, England. *Sedimentology* **35**: 671–679.
- Sarre RD. 1989. Aeolian sand drift from the intertidal zone on a temperate beach: potential and actual rates. *Earth Surface Processes and Landforms* **14**: 247–258.
- Schmutz PP. 2014. *Investigation of factors controlling the dynamics of beach surface moisture content*. PhD dissertation, Louisiana State University, Baton Rouge, LA.
- Schmutz PP, Namikas SL. 2011. Utility of the Delta-T Theta probe for obtaining surface moisture measurements from beaches. *Journal of Coastal Research* **27**: 478–484.
- Schmutz PP, Namikas SL. 2013. Measurement and modeling of moisture content above an oscillating water table: implications for beach surface moisture dynamics. *Earth Surface Processes and Landforms* **38**: 1317–1325.

- Sherman DJ, Jackson DWT, Namikas SL, Wang J. 1998. Wind-blown sand on beaches: an evaluation of models. *Geomorphology* **22**: 113–133.
- Smit Y, Ruessink G, Brakenhoff LB, Donker JJA. 2018. Measuring spatial and temporal variation in surface moisture on a coastal beach with a near-infrared terrestrial laser scanner. *Aeolian Research* **31**: 19–27.
- Stockdon HF, Holman RA, Howd PA, Sallenger AH Jr. 2006. Empirical parameterization of setup, swash and runup. *Coastal Engineering* **53**: 573–588.
- Tsegaye TD, Tadess W, Coleman TL, Jackson TJ, Tewolde H. 2004. Calibration and modification of impedance probe for near surface soil moisture measurements. *Canadian Journal of Soil Science* **84**: 237–243.
- Tuller M, Or D. 2005. Water retention and characteristic curve. In *Encyclopedia of Soils in the Environment*, Hillel D (ed), Elsevier: Oxford, UK; 278–289.
- Turner IL. 1993. Water table outcropping on macro-tidal beaches: a simulation model. *Marine Geology* **115**: 227–238.
- Turner IL, Coates BP, Acworth RI. 1997. Tides, waves and the super-elevation of groundwater at the coast. *Journal of Coastal Research* **13**: 46–60.
- Turner IL, Nielsen P. 1997. Rapid water table fluctuations within the beach face: implications for swash zone mobility? *Coastal Engineering* **32**: 45–59.
- Van Genuchten MTh. 1980. A closed-form equation for predicting the hydraulic conductivity of unsaturated soils. *Soil Science Society of America Journal* **44**: 892–898.
- Van der Wal D. 1998. Effects of fetch and surface texture on aeolian sand transport on two nourished beaches. *Journal of Arid Environments* **39**: 533–547.
- Wiggs GFS, Baird AJ, Atherton RJ. 2004. The dynamic effects of moisture on the entrainment and transport of sand by wind. *Geomorphology* **59**: 13–30.
- Wilson GW, Fredlund DG, Barbour SL. 1997. The effect of soil suction on evaporative fluxes from soil surfaces. *Canadian Geotechnical Journal* **34**: 145–155.
- Yang Y, Davidson-Arnott RGD. 2005. Rapid measurement of surface moisture content on a beach. *Journal of Coastal Research* **21**: 447–452.
- Yang H, Rahardjo H, Leong EC, Fredlund DG. 2004. Factors affecting drying and wetting soil-water characteristic curves of sandy soils. *Canadian Geotechnical Journal* **41**: 908–920.